Tellus SERIES A DYNAMIC METEOROLOGY AND OCEANOGRAPHY
PUBLISHED BY THE INTERNATIONAL METEOROLOGICAL INSTITUTE IN STOCKHOLM

Assimilating high-resolution winds from a Doppler lidar using an ensemble Kalman filter with lateral boundary adjustment

By MASAHIRO SAWADA[1]*, TSUYOSHI SAKAI[2], TOSHIKI IWASAKI[3], HIROMU SEKO[1], KAZUO SAITO[1] and TAKEMASA MIYOSHI[4,5], [1]*Meteorological Research Institute, Tsukuba, Japan*; [2]*Miyato Farm, Tome, Japan*; [3]*Department of Geophysics, Graduate School of Science, Tohoku University, Sendai, Japan*; [4]*RIKEN Advanced Institute for Computational Science, Kobe, Japan*; [5]*Department of Atmospheric and Oceanic Science, University of Maryland, College Park, MD, USA*

(Manuscript received 29 November 2013; in final form 5 February 2015)

ABSTRACT

Monitoring severe weather, including wind shear and clear air turbulence, is important for aviation safety. To provide accurate information for nowcasts and very short-range forecasts up to an hour, a rapid-update prediction system has been developed, with a particular focus on lateral boundary adjustment (LBA) using the local ensemble transform Kalman filter (LETKF). Due to the small forecast domain, limited-area forecasts are dominated by the lateral boundary conditions from coarse-resolution global forecasts. To effectively extend the forecast lead time for the small domain, a new LBA scheme using the LETKF has been developed and assessed with three sea-breeze front cases. Observing system simulation experiments for high-resolution winds from a simulated Doppler lidar were performed with the Japan Meteorological Agency Nonhydrostatic Mesoscale Model at a horizontal resolution of 400 m and 15-minute update cycle. The results indicate that the LBA improved the forecast significantly. In particular, the 1-hour wind-speed forecast with the LBA is as accurate as the 15-minute forecast without the LBA. The assimilation of Doppler lidar high-resolution wind data with the LBA is a promising approach for very short-range forecasts up to an hour with a small domain, such as for aviation weather.

Keywords: lateral boundary, data assimilation, ensemble kalman filter, doppler lidar, nowcast and very-short-range forecast, mesoscale model

1. Introduction

For aviation safety, reliable weather forecasts with a high spatio-temporal resolution are crucial (e.g. Frech et al., 2007). It is particularly important to monitor real-time weather conditions, such as the clear air turbulence, wind shear and aircraft wake vortex, during takeoff and landing (Proctor et al., 2004). For real-time monitoring of aviation weather, Doppler lidars are used at the Haneda and Narita international airports in Japan (Yamamoto, 2009), Hong Kong International Airport (Shun and Chan, 2008) and other international airports. Doppler lidar is a powerful tool for observing three-dimensional wind fields at a high spatio-temporal resolution in clear air conditions and is suitable for aviation purposes (Ishii et al., 2007; Iwai et al., 2008, 2011). Assimilating the high-resolution observations into a numerical model enables short-range numerical forecast guidance for 1–12 hours, as, for example, in Rapid Refresh (RAP, http://rapidrefresh.noaa.gov/), an operational regional numerical weather prediction (NWP) system at the National Centers for Environmental Prediction.

Dynamical downscaling using a limited-area model (LAM) is an efficient and common approach to high-resolution NWP. Generally, this approach requires an initial condition and lateral boundary conditions (LBCs). The LBCs are typically derived from a coarse-resolution global NWP model; the accuracy of the downscaling forecast depends on the initial and boundary data (Laprise et al. 2000). The domain size and the forecast length determine the degree to which the LBCs affect the model solution in the domain interior (Warner et al., 1997). When the forecast

*Corresponding author.
email: msawada@mri-jma.go.jp

Citation: Tellus A 2015, **67**, 23473, http://dx.doi.org/10.3402/tellusa.v67.23473

domain is small, the LAM forecast is rapidly dominated by the LBCs (Errico and Baumhefner, 1987; Gustafsson et al., 1998). The slight change in the coarse outer-domain forecasts may cause critical differences in the inner-domain forecasts. Moreover, the downscaling forecast using the coarser resolution model may have a difficulty in representing the small-scale phenomena because the LBCs do not include the mesoscale evolution and the domain size is not sufficiently large to self-generate within a limited domain. In this case, modifying the LBCs is a way to extend the predictability of the small forecast domain.

Data assimilation has been widely used to improve the initial conditions and the LBCs at the initial time. Several studies have included LBCs as control variables in four-dimensional variational data assimilation (4DVAR) to optimise the initial conditions and, simultaneously, the LBCs (Zou and Kuo, 1996; Kawabata et al., 2007; Gustafsson, 2012). Gustafsson (2012) showed that including LBCs as control variables in 4DVAR improved the forecasts, especially in the case of strong inflow from the lateral boundary. However, these previous studies did not consider changing the forecasted LBCs beyond the assimilation window. By modifying the LBCs for the entire forecast period, we may extend the predictability of the downscaled prediction, particularly when the forecast domain is very small. Hereafter, the scheme to modify the LBCs in the forecast period is referred to as lateral boundary adjustment (LBA). Fig. 1 illustrates how the LBA works. When the LBCs gradually deviate from the natural state (e.g. lagging of the front passage and phase error of the low/high pressure systems), the forecast errors grow because the LAM forecast approaches the inaccurate LBCs (Fig. 1a). If we apply the LBA approach and optimise the LBC in the forecast, the forecast errors are closer to the modified LBCs (Fig. 1b). If the modified LBCs have smaller forecast errors than those

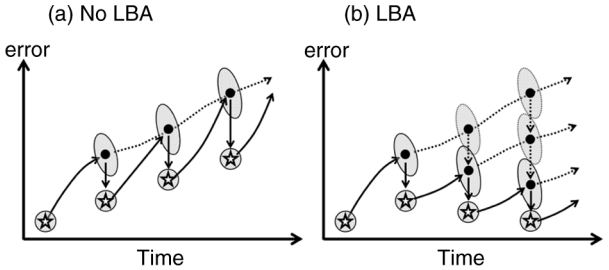

Fig. 1. Schematic of LBA. (a) without LBA and (b) with LBA. The x-axis represents the forecast time, and the y-axis is the forecast error. The stars and filled circles indicate analysis (initial conditions) and forecast (first guess), respectively. Solid arrows represent the forecast ensemble mean trajectory, and the dotted lines correspond to the LBC ensemble mean trajectory. Grey ellipses denote the ensemble spread for each analysis and forecast state.

in the original LBCs, the analysis–forecast cycle with the LBA is expected to suppress the error growth. This idea is similar to the 'quasi-outer-loop' algorithm (Yang et al., 2012), which adjusts the ensemble mean and recentres the ensemble perturbations around the adjusted more accurate mean state. We extend the recentreing of ensemble perturbations for the entire forecast period without the corresponding (future) observations (Section 2). This approach will not be a good choice if the background error covariance suddenly changes.

The purpose of this study is to develop a rapidly updated NWP system combined with LBA for a very short-range forecast ($\sim$1 hour) and to assess its impact on forecasts in an observing system simulation experiment (OSSE) with Doppler lidar. We use the local ensemble transform Kalman filter (LETKF, Miyoshi and Aranami, 2006; Hunt et al., 2007; Miyoshi and Kunii, 2012) to develop the LBA scheme. The paper is organised as follows. Section 2 describes the newly developed LBA scheme, followed by the experimental design in Section 3. Section 4 presents the results. Finally, Section 5 provides concluding remarks and discussions.

2. Lateral boundary adjustment

The LBA scheme corrects the ensemble mean of the LBCs for the entire forecast period using the LETKF. First, we introduce a basic equation of LETKF, which is used for providing an initial condition of forecast–analysis cycle. Then a specific equation for LBA proposed in this study is introduced.

In the LETKF, the analysis equation for the ensemble mean state is (e.g. Hunt et al., 2007; Miyoshi, 2010) as follows:

$$\bar{x}_i^a = \bar{x}_i^f + \delta \mathbf{X}_i^f \bar{w}_i, \tag{1}$$

$$\bar{w}_i = \widetilde{\mathrm{P}}_i^a (\mathrm{H}\delta \mathbf{X}_i^f)^T \mathrm{R}^{-1} (y_i^o - \overline{H(x_i^f)}), \tag{2}$$

where x is the model state variable and δX is the ensemble perturbation matrix (each column corresponds to each member). w_i is the weight matrix or transformation matrix. $\widetilde{\mathrm{P}}^a$ is the analysis error covariance matrix in the space spanned by analysis ensemble perturbations and **R** is the observation error covariance matrix. H is the observation operator, **H** is its tangent linear and y° is the observation. The overbar denotes the ensemble mean. Superscripts a and f represent analysis and forecast, respectively, and the subscript i is the time index. The second term on the right-hand side of eq. (1) is known as the analysis increment. Practically, the analysis ensembles for the initial condition are constructed by adding analysis ensemble perturbations $\delta \mathbf{X}_i^f w_i$ to the forecast ensemble mean $\bar{x}_i^f$ (Bishop et al., 2001; Hunt et al., 2007; Miyoshi, 2010).

Following this, the LBA equation is derived based on eq. (1) by assuming that the transformation matrix w_i remains constant for the entire forecast period. This assumption can be made, because the forecast time is very short (several hours at most) and the transformation matrix cannot be obtained satisfactorily for the entire forecast period without the corresponding (future) observations y_n° $(n > i)$. Additionally the computational cost can be saved by reducing the matrix operation. Based on this assumption, we obtain the analysis ensemble mean for the entire forecast period:

$$\bar{x}_n^a = \bar{x}_n^f + \delta \mathrm{X}_n^f \bar{w}_i, \tag{3}$$

Here, the subscript n is the index for the forecast time step from i+1 to N (end of forecast). Moreover, eq. (3) is identical to eq. (1) at $n = \mathrm{i}$ (analysis time). The ensemble mean of the LBCs for the forecast period ($\bar{x}_n^f$) is modified using eq. (3). The lateral boundary perturbations (LBPs) are derived from the ensemble downscaling forecasts of coarse-resolution global NWP. Thus the LBCs (x_n^a) are obtained: $x_n^a = \bar{x}_n^a + \delta \mathrm{X}_n^f$.

3. Experimental design of OSSE

An OSSE was performed to assess the impact of the LBA scheme. The OSSE consisted of the LETKF data assimilation system based on the Japan Meteorological Agency Nonhydrostatic Model (JMA-NHM), nature run (TRUE), simulated Doppler lidar observations and ensemble downscaling forecasts. An outline of the OSSE experimental design is presented in Table 1. The nature run was performed with the JMA-NHM, a mesoscale model developed by JMA, operational since March 2006 (Saito et al., 2007). Previous studies have applied the LETKF to the JMA-NHM with promising results (Miyoshi and Aranami, 2006; Seko et al., 2011; Saito et al., 2012). In the present study, the nature run was created by downscaling the JMA operational mesoscale analysis at a 10-km resolution to a 0.4-km resolution, at 3-hourly intervals. A horizontal resolution of 0.4 km was necessary to resolve sea-breeze front sharply in this case. The simulation was run for 168 hours, starting at 09 LT on June 16, 2007. The nature run data consisted of meteorological fields every 15 minutes. The computational domain contained 72×72 horizontal grid points and 40 vertical layers. For the lateral boundaries, a sponge layer with eight grids on each boundary was employed. The eastern and western boundaries covered the ocean and the land regions, respectively (Fig. 2b).

To create the LBPs for the analysis–forecast cycles with LETKF, ensemble downscaling forecast experiments were performed using the JMA operational 1-week ensemble prediction system (EPS) with a horizontal resolution of 1.25° and 6-hourly intervals. The unperturbed and the first 10 positive perturbed members were used for the initial and LBCs, downscaled to horizontal resolutions of 12 km and 2 km, with one-way nesting. By subtracting the first 10 positively perturbed members from the unperturbed member, 10 negatively perturbed members were obtained; the entire forecast ensemble, with a 0.4-km mesh, included 21 members. The forecast length and output interval, in the experiment with a 2-km mesh, were the same as those in the TRUE.

In the OSSE, the lidar observations were simulated from the TRUE fields through interpolation at the observation locations, assuming a lidar specification similar to that used at the Sendai airport (Iwai et al., 2008). The simulated lidar performed plane position indicator (PPI) scans at 20 distinct

Table 1. Outline of the experimental design for OSSE

	Resolution	Duration (LT)	Member
TRUE	0.4 km	9:00 LT 16–9:00 LT 23 July 2007	1
LBP	2 km	9:00 LT 16–9:00 LT 23 July 2007	21
LETKF for initial conditions	0.4 km	14:15–18:00 LT 16 July 2007 06:15–10:00 LT 17 July 2007 05:15–09:00 LT 19 July 2007	21
LBA	2 km	14:15–18:00 LT 16 July 2007 06:15–10:00 LT 17 July 2007 05:15–09:00 LT 19 July 2007	21
Forecast cycle	0.4 km	14:00–18:00 LT 16 July 2007 06:00–10:00 LT 17 July 2007 05:00–09:00 LT 19 July 2007 Each forecast starts with 15 minutes interval	21
Extended forecast experiments	0.4 km	14:00–18:00 LT 16 July 2007 06:00–10:00 LT 17 July 2007 05:00–09:00 LT 19 July 2007 Each 1-hour forecast starts with 15 minutes interval. See the detail in Section 4.2.	21

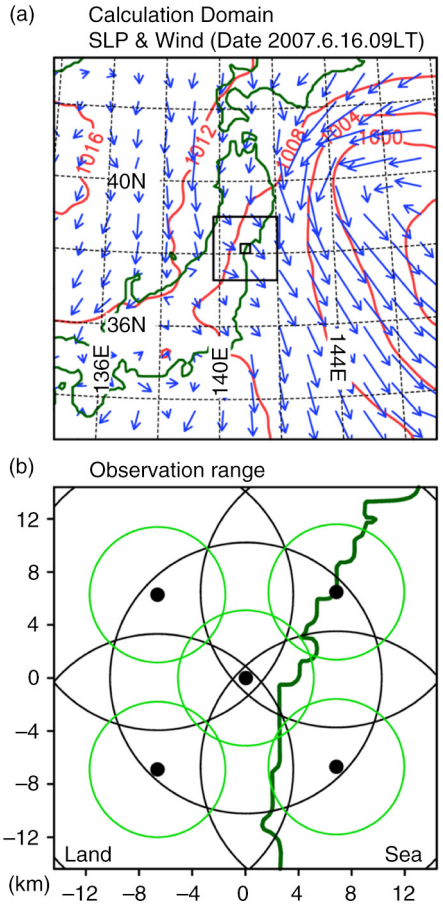

Fig. 2. (a) Calculation domain for the 12-, 2- and 0.4-km horizontal resolutions (solid squares), and surface weather map. Green lines correspond to the coastline. Red contours and arrows represent sea-level pressure and surface wind at 09:00 LT on 16 June 2007. (b) Lidar observation range at each site in the domain for the 0.4-km horizontal resolution. Black and green circles represent the observation range from each lidar for AS/ASLB and AS_h/ASLB_h, respectively. The Sendai airport is located at $x = y = 0$.

elevation angles (i.e. 1°, 2°, 4°, 6°, 8°, 10°, 12°, 14°,17°, 20°, 25°, 30°, 35°, 40°, 45°, 50°, 55°, 60°, 70° and 80°) with an azimuth resolution of 18° and a radial resolution of 180 m from 360 m to 10 080 m (55 points) in the radial direction (a horizontal range of observations is shown in Fig. 2b). The radial resolution used by Iwai et al. (2008) was 90 m but the number of elevation angles increased by decreasing radial resolution to produce spatially uniform observation data. The observed height is limited to below an altitude of 2 km. The total number of lidar observations was 12 860. A simulated lidar observation was generated every 15 minutes, for 168 hours. Gaussian random errors, with standard deviations of 1 m s^{-1}, were added to the radial velocity. The simulated lidar data were generated with the same grid spacing as the forecast experiment such that the representativeness error, unlike the real situation, was not included.

The LETKF data assimilation scheme (Miyoshi and Kunii, 2012) was adjusted to the JMA-NHM through several modifications, including the implementation of vertical hybrid coordinates and the introduction of LBPs in the forecast–analysis cycles. The state vector incorporated air density, u, v, w, temperature, pressure, water vapour mixing ratio, surface pressure, ground temperature, underground temperature and surface precipitation. The assimilation cycle for the initial conditions was conducted with a horizontal resolution of 0.4 km and an assimilation window of 15 minutes. The 15-minute forecast with a horizontal resolution of 0.4 km was used as a first guess. Simulated observation data were assimilated during the analysis. The ensemble size was set to 21, and a multiplicative inflation factor of 10% was used. The localisation parameters of LETKF were set to 2 km in the horizontally and 0.5 km in the vertically.

The LBA was conducted using only the ensemble perturbations with the 2-km mesh (LBPs), because the ensemble perturbations with the 0.4-km mesh for the entire forecast period could not be obtained before the analysis–forecast cycle was completed. The horizontal localisation parameter of the LBA was set to 50 km, modifying the LBCs, even though the lidar data were far from the lateral boundary; the horizontal localisation parameter of 2 km is too short to modify the LBCs. The localisation radius of influence is $2\sqrt{10/3}$ times the localisation parameter (Gaspari and Cohn, 1999; Hamill et al., 2001). The vertical localisation parameter was fixed at 0.5 km. A super-observation method was applied in order to reduce the computational time for the assimilation cycle and the random instrumental error. Super-observations are generally applied to higher-resolution observation data (180 m, in the present study) than the model grid spacing (2 km). The simulated radial velocity was interpolated to the 2-km horizontal grid using the Cressman scheme (Seko et al., 2004).

Table 2 presents an outline of the three experiments (and additional sensitivity experiments) performed in order to examine the effect of LBA. The first experiment was a pure ensemble forecast from the JMA 1-week EPS without assimilation (NOAS), aimed at obtaining the impact through comparison with the two subsequent experiments. The second experiment was an analysis–forecast cycle using the simulated lidar data to correct only the initial conditions (AS). The third experiment was an analysis–forecast cycle with LBA, aimed at correcting both the initial conditions and the LBCs (ASLB). This final experiment required twice the assimilation processing for each analysis cycle, one for the initial conditions and another for the LBCs (LBA). The model setting (resolution and physical parameterisations) in the three experiments were the same as those in TRUE.

Table 2. List of experiments

Name	Description
NOAS	Forecast without assimilation
AS(AS1p)	Analysis-forecast cycle without LBA
ASLB(ASLB1p)	Analysis-forecast cycle with LBA
AS2p, 4p	Same as AS except with 2, or 4 lidar instruments
ASLB2p, 4p	Same as ASLB except with 2, or 4 lidar instruments
AS2p_h, 4p_h	Same as AS2p, 4p except with half of lidar observation range
ASLB2p_h, 4p_h	Same as ASLB2p, 4p except with half of lidar observation range
F1h_AS	1-hour forecast from the analysis of AS
F1h_ASLB	1-hour forecast from the analysis of ASLB

The resolution, domain size, output interval and physical parameterisations are the same as those in the TRUE.

Three study cases were selected (Table 3): 14:00–18:00 LT on June 16, 06:00–10:00 LT on June 17 and 05:00–09:00 LT on June 19 2007; based on the changes in wind direction associated with the passage of a sea-breeze front in the TRUE fields. These targets were considered appropriate, because the lidar observation system provides a very high spatio-temporal resolution of short-range radial winds; effectively detecting the detailed structure and precise timing of the frontal passage. During the period 14:00–18:00 LT on June 16, 2007, synoptic westerlies were prevailing over the Sendai airport, with wind speeds greater than 10 m s^{-1} at the 500-m height. The westerlies weakened gradually, and a sea-breeze intrusion with a clear front was observed in the late afternoon. During the period 06:00–10:00 LT on June 17, 2007, a sea-breeze with an approximately 400 m thickness developed under calm conditions. Finally, northwesterlies at 5–7 m s^{-1} formed a sea-breeze with a thickness of approximately 200 m during the period 05:00–09:00 LT on June 19, 2007. The experiments were performed for 4 hours in each case.

4. Results

4.1. A case study with and without the LBA

As noted above, previous studies have suggested that the forecast error in the LAM is restricted by the LBCs. To overcome the limitation of the LBCs, this study attempted to optimise the LBC by applying the LETKF to forecasted variables of the LBC in the OSSE framework. First, one case study was described in detail. Then, a composite of the three cases was analysed. Fig. 3 shows simulated wind fields at a 125-m height for the case 14:00–18:00 LT on June 16, 2007, for TRUE, NOAS, AS and ASLB. Vectors and shaded regions represent the horizontal wind and east–west wind speed at a 125-m height, respectively. Ensemble means in NOAS and analysis means in AS and ASLB are displayed. In this case, a low-pressure system moved from the southwest to the east coast of Japan, which caused the prevailing northwesterly winds (Fig. 2a). The prevailing northwesterlies gradually weakened in the afternoon; the sea-breeze front passed the Sendai airport at 17:00 LT in the surface weather observation. In the TRUE wind field, the sea-breeze front appeared at the eastern boundary at 15:30 LT, intruded over land at 17:00 LT and reached the Sendai airport at 17:15 LT (not shown). In the NOAS experiment, the sea-breeze had already penetrated the inland area at 15:00 LT because the synoptic westerlies were weaker than those of TRUE due to the weaker low-pressure system. In the AS experiment, the synoptic northwesterlies, which were not formed in NOAS, were formed successfully, and the sea-breeze was not observed at 15:00 LT. At 16:00 LT, the sea-breeze penetrated the boundary, arising from the excessive easterlies of the LBCs, as shown for NOAS in Fig. 3. The position of the sea-breeze front was obscure at 17:00 LT. The passage of the sea-breeze front at the Sendai airport was successfully captured. However, the front over-penetrated near the northern and southern lateral boundaries due to excessive easterlies in the LBC at 18:00 LT. The ASLB experiment also captured the right timing and position of the sea-breeze intrusion similar to AS. At 15:00 LT, the excessive easterlies at the eastern lateral boundary became weaker than in AS. At 16:00 LT, the excessive

Table 3. Outline of case studies

Name	Case 1	Case 2	Case 3
Duration	14:00–18:00 LT 16 July 2007	06:00–10:00 LT 17 July 2007	05:00–09:00 LT 19 July 2007
Representation of TRUE	Westerly more than 10 m s^{-1}, clear sea-breeze front.	Calm condition (<2 m s^{-1}), sea-breeze is 400 m thickness.	Northwesterly of 5–7 m s^{-1}, sea-breeze is 200 m thickness.

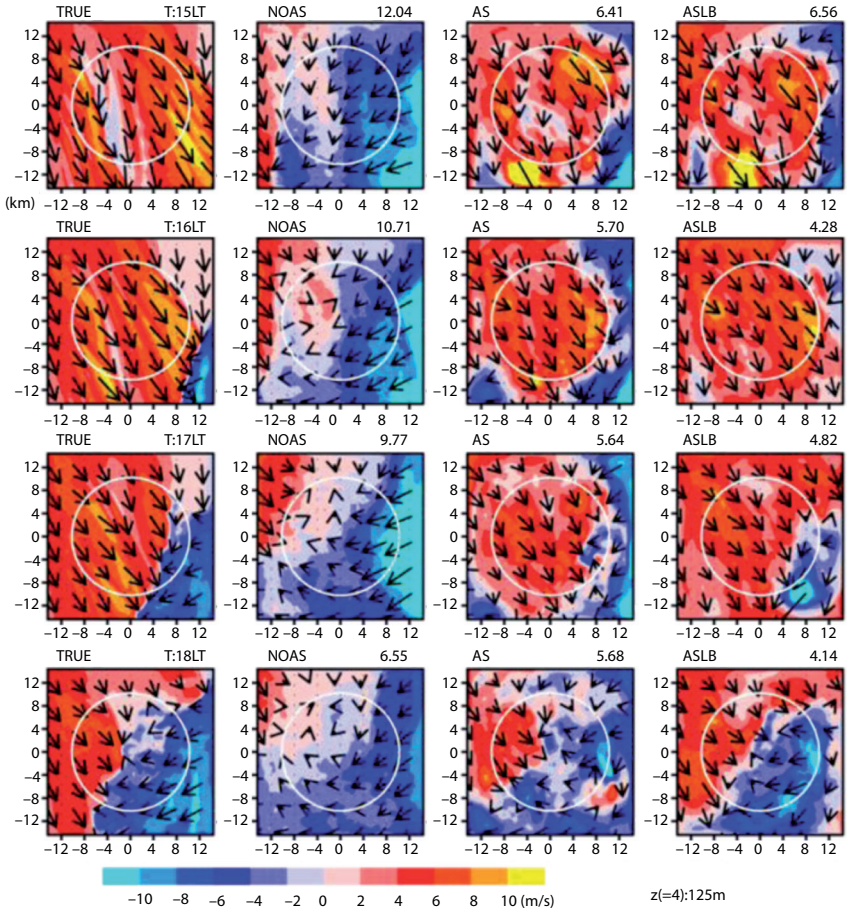

Fig. 3. Horizontal wind (arrows) and the structure of east–west wind speed (shades) at 125-m height. From the left panels, TRUE, NOAS, AS and ASLB are displayed with 1-hour interval. Panels of AS and ASLB are analysis ensemble mean. Numbers on the upper right corner of each panel indicate UTC for TRUE and area-averaged RMSEs for NOAS, AS and ASLB. Circle in each figure denote the observation range. The x- and y-axes are the distance from the centre of calculation domain.

easterlies along the northeastern lateral boundary were reduced through the assimilation cycle. However, the sea-breeze near the southeastern lateral boundary was not captured because it was located outside the observation range of the lidar. One hour later, the sea-breeze front was within the observation range; the front structure was then well captured. The sea-breeze front was clearly formed at 18:00 LT and, unlike AS, the excessive penetration of the sea-breeze near the northern and southern lateral boundaries did not occur. The easterlies at the eastern lateral boundary were weaker than in the TRUE fields, possibly because the LBA uses a long horizontal localisation parameter so that both the westerlies and easterlies near the centre were assimilated.

The vertical structures of the simulated sea-breezes are examined from east–west cross sections at $y = 0$ km for 1-hour intervals in Fig. 4. Thick lines represent contour lines of east–west wind speeds of 0 m s^{-1}, indicating the boundary between the sea-breeze and synoptic flows for the TRUE fields. The sea-breeze appeared at the eastern lateral boundary approximately 16:00 LT, and its front, with a thickness of less than 400 m, travelled inland at a speed of 2–3 m s^{-1}, passing the Sendai airport ($x = 0$ km) at 18:00 LT in the TRUE data. The sea-breeze (easterly) with a thickness of 600–800 m penetrated inland in the NOAS experiment at 15:00 LT and remained until 18:00 LT. The NOAS experiment failed to reproduce the sea-breeze thickness and the timing of its intrusion. The sea-breeze position and thickness were well captured between 17:00 and 18:00 LT in both AS and ASLB because of the assimilation of lidar data. These cases reproduced the synoptic westerlies, which were not formed in NOAS. Compared with AS, a stronger sea-breeze near the surface was found in ASLB, similar to the TRUE fields.

To investigate the extent to which the LBA reduces the forecast and analysis errors, the horizontal map of root-

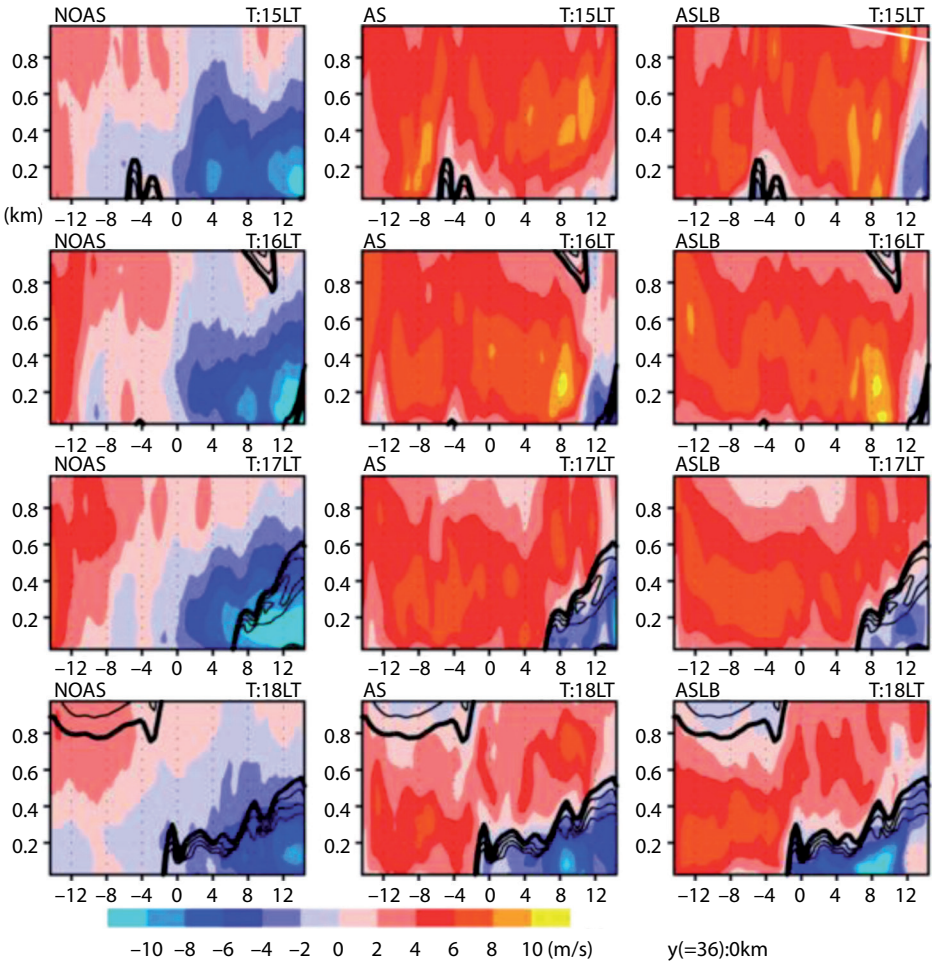

Fig. 4. Sea-breeze vertical structures with time interval of 1 hour in the NOAS, AS and ASLB. Panels of AS and ASLB are analysis ensemble mean. Shades indicate east–west wind speed at y = 0 km. Contours denote east–west wind speed with the values of −6, −4, −2, 0 m s^{-1} in the TRUE. Thick contours indicate the boundary between sea-breeze and westerly.

mean-square errors (RMSEs) for both wind speed and direction are shown for the NOAS, AS and ASLB experiments in Fig. 5. The RMSE was calculated as follows:

$$\mathrm{RMSE} = \sqrt{\frac{1}{\mathrm{NT} \times \mathrm{NZ}} \sum_{t=1}^{\mathrm{NT}} \sum_{z=1}^{\mathrm{NZ}} \{(\mathrm{U} - \mathrm{Ut})^2 + (\mathrm{V} - \mathrm{Vt})^2\}},$$

where U and V are ensemble mean east–west and north–south wind speeds, respectively, in NOAS, AS or ASLB and Ut and Vt are TRUE fields. z and t are indexes for the vertical layer and time step, respectively. Here, NZ is 20, which corresponds to a 1-km height; NT is 16 for the period 14:15–18:00 LT, with an interval of 15 minutes (16 assimilation cycles). The NOAS experiment had the largest RMSE over the entire domain, especially along the southern lateral boundary, where the excessive progression of the sea-breeze front was observed. In both first guess and analysis fields of AS, the RMSEs became 2–3 m s^{-1} smaller inside the lidar observation range than near the lateral boundaries. The RMSEs of the first guess near the inflow lateral boundaries were close to those in NOAS because both experiments employed the same LBCs. The RMSE near the lateral boundaries was remarkably smaller in the first guess and analysis of ASLB than in those of AS. In the southwest quadrant, the RMSEs of both the first guess and analysis of ASLB decreased by more than half of the AS experiment. Another important difference is that the RMSE in the domain interior decreased in the first guess of ASLB. For the first guess, the LBA had a positive impact on the forecast not only near the lateral boundaries but also in the inner area.

To evaluate the temporal changes of forecast error in the three experiments for 14:00–18:00 LT on June 16, 2007, domain-averaged RMSEs of wind speed below 1 km are shown in Fig. 6. The lines represent both the first guess and analysis RMSEs. In the NOAS experiment, the RMSE

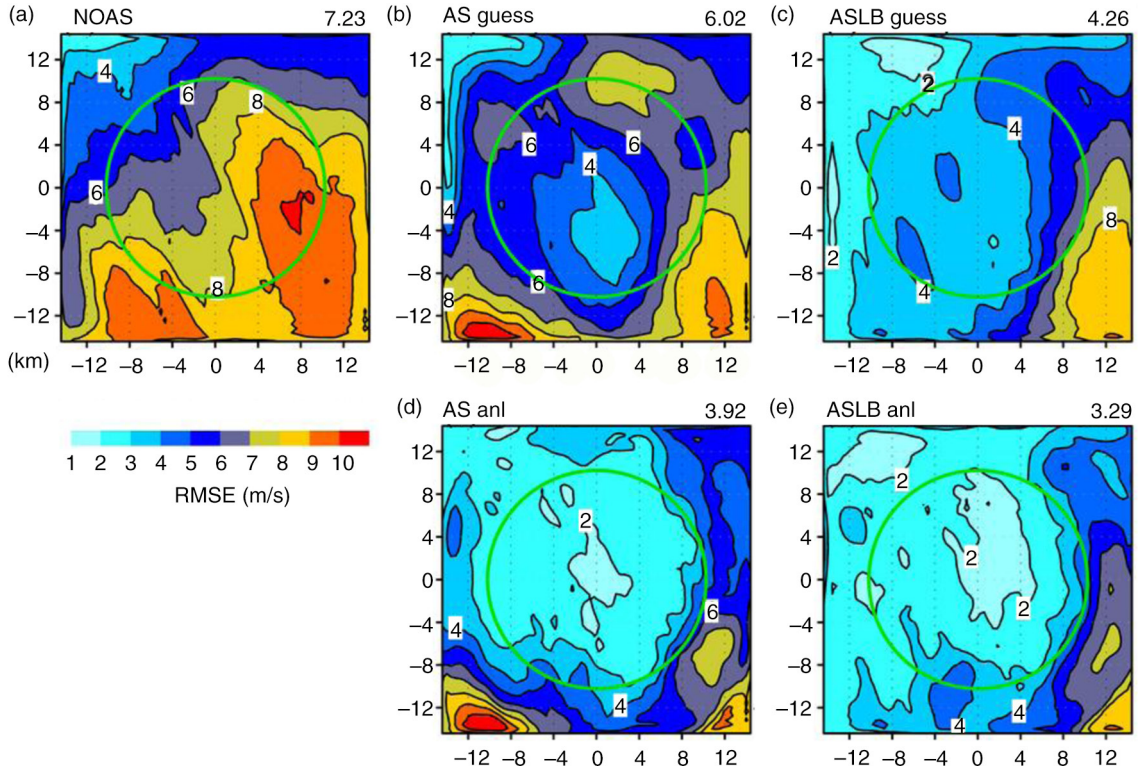

Fig. 5. Vertically averaged RMSE of wind speed, from surface to 1-km height in the NOAS, AS and ASLB. For the AS and the ASLB, first guess and analysis are displayed. Circle in each figure denote the observation range.

reached approximately 8.5 m s^{-1} at 15:15 LT, gradually decreasing thereafter to 6 m s^{-1}. The RMSE for the analysis in AS was smaller than that in the NOAS. However, the error rapidly grew from the lateral boundaries (Fig. 5b), approaching the NOAS error. This pattern is consistent with the findings of previous studies (c.f. Errico et al., 1993). The assimilation reduced the temporally averaged RMSEs of the first guess and analysis for the period 14:15–18:00 LT in AS by 6.19 m s^{-1} and 4.03 m s^{-1}, respectively. When the LBA was applied, the RMSEs for the analysis and first guess of ASLB became 2.39 m s^{-1} (39%) and 0.91 m s^{-1} (23%) smaller, respectively, than those in the AS. In ASLB, the RMSE for the first guess increased by less than 1 m s^{-1} from the analysis for the entire period. It is evident that the RMSE reduction for the first guess arises from the LBA, indicating that this has a positive effect on the extended forecast.

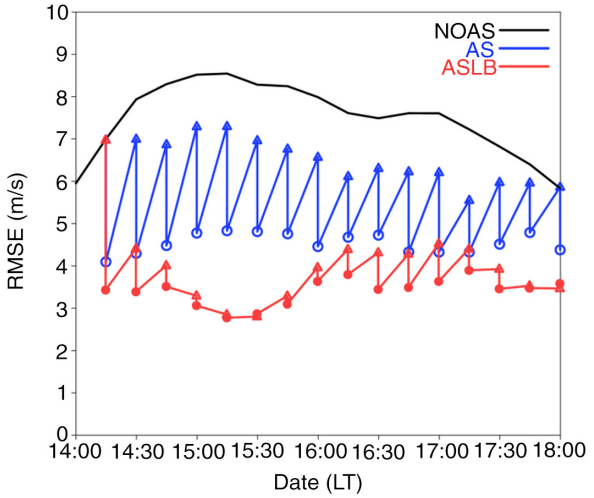

Fig. 6. Domain-averaged RMSE of wind speed from surface to 1-km height for the analysis–forecast cycle in the NOAS (black), AS (blue) and ASLB (red). The x-axis denotes the forecast date and the y-axis is the averaged RMSE. Circles and triangles represent analysis and first guess.

4.2. *Extended forecast experiment*

The effectiveness of the LBA in extending the forecast lead time was quantitatively investigated with additional experiments. The forecasting processes were extended from 15 minutes to 1 hour at each analysis time (15-minute intervals) for the three cases with and without the LBA. Hereafter, these experiments are called F1h_AS and F1h_ASLB. The model setting (resolution and physical parameterisations) in the extended forecast experiments were the same as

those in the TRUE. Figure 7 shows the time-series of the domain-averaged wind-speed RMSEs for each forecast at different initial times (14:00 LT, 06:00 LT and 05:00 LT on June 16, 17 and 19, 2007, respectively). The circles represent the initial time, and blue and red lines correspond to F1h_AS and F1h_ASLB, respectively. The values are normalised by the NOAS RMSE at each forecast time. These panels demonstrate that the error growth rate depends significantly on the specific cases, especially in the F1h_AS scenario. In case-1 of the F1h_AS simulation, the normalised RMSE was 0.6 at the initial stage (analysis), exceeding unity (the NOAS RMSE) in the 30-minute forecast. In case 2 of F1h_AS, the RMSE rapidly increased and exceeded the NOAS RMSE after 15 minutes. This result may be caused by a dynamical inconsistency between the assimilated interior flows and the LBC. The RMSE grew relatively slower in case 3 of F1h_AS, approaching the NOAS RMSE. A particularly interesting result is that the RMSE became significantly smaller in F1h_ASLB than in F1h_AS for all initial times and cases. In almost all cases, the RMSE at 1 hour was smaller than the NOAS RMSE except for a few initial points in case-1. This difference is because the wind direction changed from a synoptic westerly to a sea-breeze (easterly) at the southeastern boundary, outside of the lidar observation range, during the period 16:15–17:00 LT (Fig. 3). Even though the lidar data without the information on the wind direction change were assimilated, the LBA could not reproduce suitable LBCs, resulting in a large RMSE in that region.

Figure 8 illustrates the normalised error growth by the NOAS RMSE. The two lines with one standard deviation bar are the averaged RMSE for the 36 forecast experiments, which consist of three cases, with each case with 12 1-hour forecast experiments from different initial times. In F1h_AS, the normalised RMSE was less than 70% of the NOAS RMSE at the initial time and increased to unity after 15 minutes, which means the RMSE is comparable with the NOAS RMSE. The normalised RMSE in F1h_AS was approximately constant for the 30- to 60-minute forecasts because the LBC controls the domain interior during this period. The normalised RMSE in F1h_ASLB at the initial time was less than 40% of the NOAS RMSE and grew quite slowly with time, reaching a normalised RMSE of 0.48 ± 0.23. The 1-hour forecast error in F1h_ASLB was smaller than at the initial time in F1h_AS. It is evident that the LBA contributes to extending the forecast lead time in this study.

The horizontal distributions of normalised RMSE in F1h_AS and F1h_ASLB are presented in Fig. 9. Shaded regions represent the normalised RMSE, and contours represent the RMSE for the 15-minute (Fig. 9a, c) and 60-minute (Fig. 9b, d) forecast lengths. The 15-minute forecast of F1h_AS shows that the normalised RMSE became less

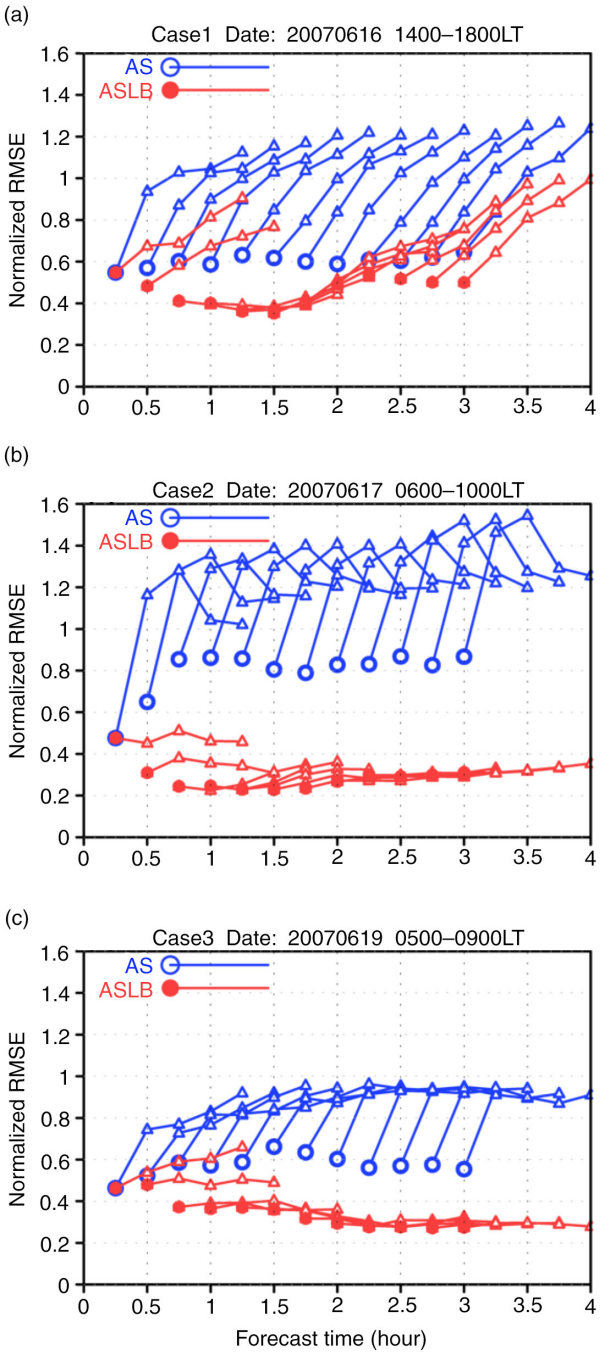

Fig. 7. Domain-averaged normalised RMSEs by the RMSE of NOAS at each forecast which have different initial times in the three cases. Circles and triangles represent analysis and first guess. Blue and red lines indicate F1h_AS and F1h_ASLB experiments.

than 0.8 within half of the lidar observation range and was comparable with that of the NOAS RMSE along the lateral boundaries. For the 1-hour forecast, there was no improvement in nearly the entire domain, indicating that the effects of assimilated initial conditions quickly disappear.

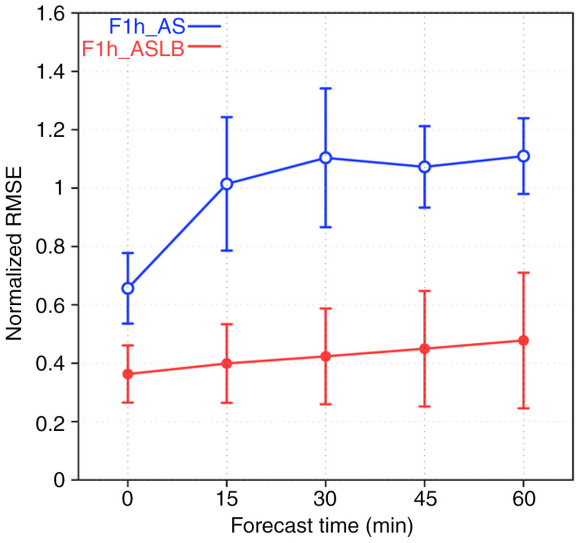

Fig. 8. The ensemble averaged normalised error growth by the NOAS. Blue and red lines indicate F1h_AS and F1h_ASLB experiments. Bars over the circles indicate one standard deviation. The x-axis corresponds to the forecast length from analysis.

The RMSE of the 15-minute forecast in F1h_ASLB was less than 0.4 of the NOAS RMSE near the lateral boundaries and within the lidar observation range, representing a significant improvement compared with F1h_AS. The RMSE distribution for the 1-hour forecast was similar to that of the 15-minute forecast, revealing that the forecast error did not grow quickly through the lateral boundaries in F1h_ASLB. In this study, the LBA was effective for the 1-hour forecast length and suppressed the error growth throughout the entire forecast domain.

4.3. Additional experiments on the observation range and number of instruments

The impacts of the number of instruments and observation range on the forecast error were investigated by performing several sensitivity experiments. Two and four lidar observation sites were deployed (Fig. 2b), referred to as AS2p and AS4p, respectively. The model setting (resolution and physical parameterisations) in the sensitivity experiments were the same as those in the TRUE. Domain-averaged RMSEs are presented for the observation range of approximately 10 km and 5 km from the lidar in Fig. 10. RMSEs are averaged for the three cases. As the number of lidars increased, the RMSEs of analysis decreased in all experiment cases. In the analysis of AS, the RMSE reduction in response to the increase in lidars was larger than in ASLB. However, the RMSEs for the first guess of AS did not decrease as suggested by the analysis when the number of lidars increased. Despite the AS4p covering the entire extent of the lateral boundaries, the forecast error grew quickly and became comparable to the NOAS RMSE after 15 minutes, which suggests that the initial condition correction was not sufficient to reduce the forecast error. The RMSE for the first guess was smaller in ASLB1p than in AS4p, implying that the LBA effectively uses past observation information because the error reduction was larger in ASLB than in AS even though there were fewer observations in ASLB.

To investigate the impacts of the observation range radius, we performed sensitivity experiments with half the observation range of AS and ASLB, referred to as AS_h and ASLB_h, respectively. The RMSE for the analysis was 0.5–1.5 m s^{-1} larger in AS_h and ASLB_h than in AS and ASLB because the observation coverage was small in the AS_h and ASLB_h experiments. The RMSE for the first guess of AS_h was similar to that of AS, which was caused by saturation of the forecast error produced by the LBC. In contrast, the RMSE for the first guess of ASLB_h became 1.2–1.6 m s^{-1} larger than in ASLB. The effects of the number of instruments in AS_h and ASLB_h were nearly qualitatively the same as in AS and ASLB. In these cases, the results imply that the LBA, rather than increasing the number of lidars and observation range, is required to extend the forecast lead time because the RMSE was dominated by the lateral boundaries rather than the initial conditions.

5. Conclusion and discussion

We have proposed an LBA scheme using the LETKF and evaluated its effectiveness at extending the forecast lead time for three cases in which a sea-breeze was formed by performing OSSE using Doppler lidar. The RMSEs for the first guess and analysis of AS decreased by 1.0 and 3.2 m s^{-1} (14 and 44%), respectively, compared with the RMSE of NOAS. By applying the LBA, the RMSEs were 3.4 and 4.1 m s^{-1} (47 and 57%) smaller than that in NOAS and were 2.4 and 0.9 m s^{-1} (39 and 23%) smaller than in AS, respectively. Compared with the AS, the RMSE was clearly reduced in the first guess because the LBA reduced the RMSE both in the domain interior and near the lateral boundaries. Forecast experiments for 1 hour were performed at each analysis time (12 initial times for one case) for the three cases to investigate the extent to which the LBA extends the forecast lead time. The domain-averaged RMSE of ASLB for the 1-hour forecast for all cases decreased by 3.5 m s^{-1} (50%) of the AS RMSE, which is less than or comparable to the RMSE of the 15-minute forecast for AS.

In previous studies and most operational centres, data assimilation is primarily used for the improvement of the initial conditions. This adjustment is not always beneficial in a LAM forecast, especially with a narrow domain, because

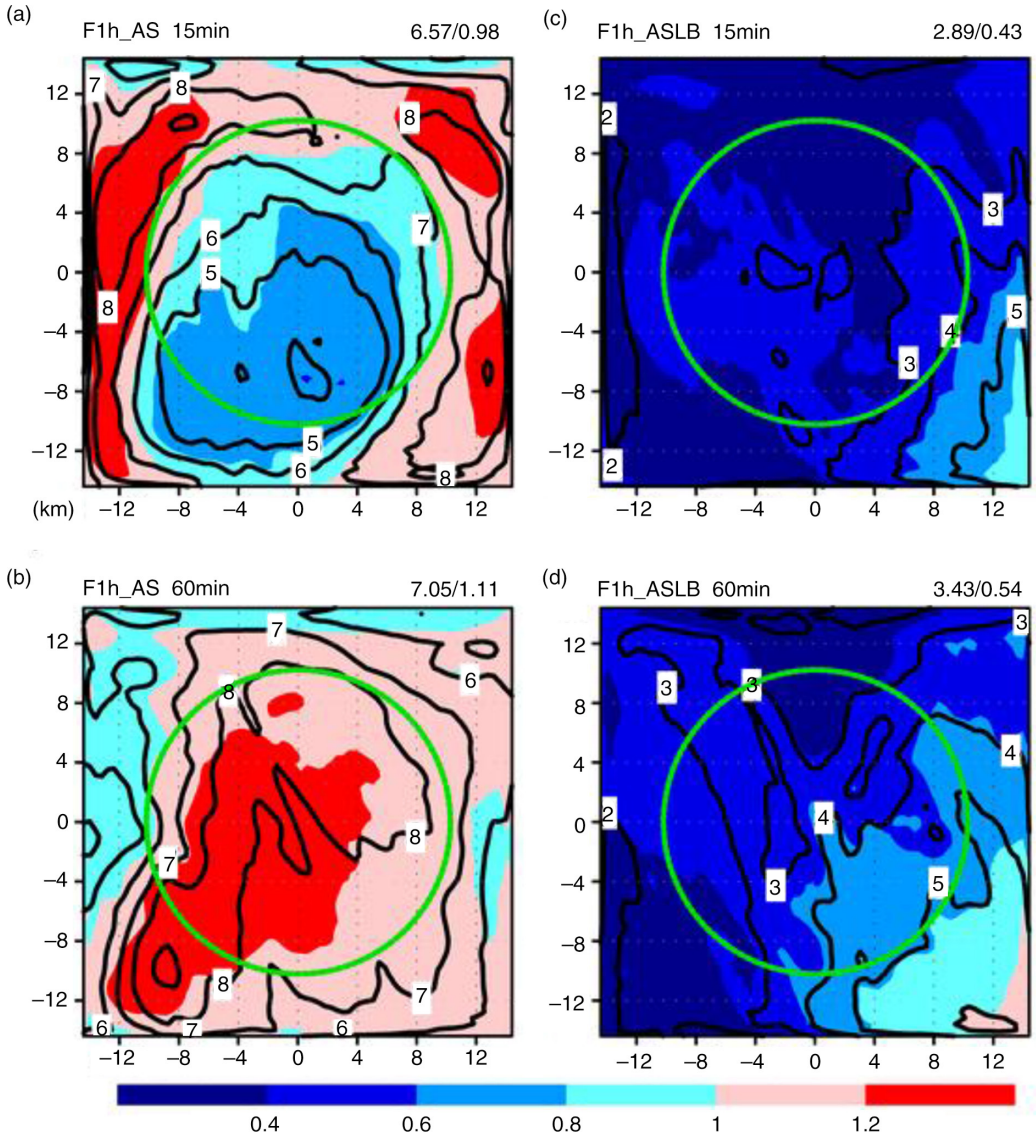

Fig. 9. Horizontal distribution of the normalised RMSE by the RMSE of NOAS in the (a), (b) F1h_AS, and (c), (d) F1h_ASLB. Upper panels refer to the 15 minutes forecast and the lower panels to the 60 minutes forecast. Contours and shades indicate the RMSE with the interval of 1 m s^{-1} and the normalised RMSE. These are averaged for 36 cases. Numbers on the upper right corner of each panel are the domain-averaged RMSE and normalised RMSE. Circle in each figure denote the observation range.

the observation information is quickly lost from the lateral boundaries (Warner et al., 1997). We accomplished an extended forecast for a narrow domain under the OSSE framework based on the assumption of linearity of the analysis increment during a forecast period ($\sim$1 hour in this study). To the best of the authors' knowledge, this method is the first LETKF attempt to mitigate the error growth from LBCs, and the findings indicate that the proposed LBA is a promising approach for prediction for narrow domains. The combination of prediction, Doppler lidar and data assimilation with LBA will be useful for providing not only aviation hazard guidance but also severe weather (tornado and torrential rain) and situational awareness information.

In the operational sense, a caution may be needed with regard to the computational cost. The ASLB experiment requires double assimilation for each analysis, increasing the computational demand compared with AS (one assimilation for each analysis). However, the assimilation uses only less than 5% of the total CPU time of 20-member ensemble runs in this configuration. Therefore, the additional assimilation computation is not essential.

Another concern is that the remarkable improvement after applying the LBA may be related to the non-normalised LBP. Here, the LBP was produced from the dynamical

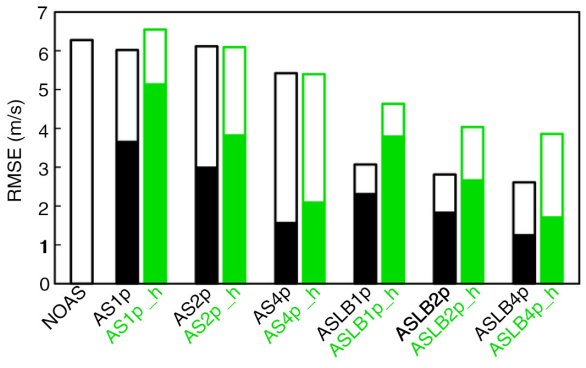

Fig. 10. The domain-averaged RMSEs of wind speed in the NOAS, AS1p, AS2p, AS4p, ASLB1p, ASLB2p, ASLB4p, AS1p_h, AS2p_h, AS4p_h, ASLB1p_h, ASLB2p_h and ASLB4p_h. Filled and open bars indicate analysis and first guess (15-minute forecast) errors, respectively. The y-axis is RMSE (unit is m s^{-1}).

downscaling from the JMA global ensemble forecast, in which the spread is too large because the forecast time is different from the small-domain forecast. The large LBP causes the ensemble spread to increase, resulting in an excessive correction by the observations. We may need to consider generating an appropriate LBP (c.f. Torn et al., 2006; Saito et al., 2012). This will remain an important future issue. The assumption of constant background error covariance matrix during the whole forecast period is also shortcoming because it may lose the flow-dependent characteristics, leading to filter divergence. Throughout this work, the assumption of constant $\delta \mathbf{X}_i^f$ is valid at least for the selected dry cases. Additionally, the lidar observation is only assimilated in the limited-area domain, possibly leading to the significant improvement. It is necessary to evaluate a combinational effect between the lidar observation and other instruments, such as surface observation, which could reduce the impact of assimilation with lidar observation. The LBA is effective only in some rare cases with a large forecast displacement error such as in this study.

Similarly to the LBA approach, parameter estimation techniques based on data assimilation could be applied to produce the LBCs at appropriate forecast time. Parameter estimation generally provides optimal parameters (LBCs in the present case) at the analysis time using the present observations. If the idea of the four-dimensional ensemble Kalman filter (Hunt et al., 2004) is applied to parameter estimation, parameter values at the later forecast times can be estimated with the present observations; this is analogous to the LBA approach. Similar assumptions are made by the running-in-place method (Kalnay and Yang, 2010), and quasi-outer-loop method (Yang et al., 2012). These methods improve state estimates using the 'future' observations within the assimilation window. The parameter estimation and the LBA can be considered as a similar approach.

Although the preliminary results from this case study provide a promising approach to exploring how the LBCs improve LAM predictions, future work is required to practically implement the proposed LBA. Because only three study cases with very specific condition (only assimilated lidar data without other observations and large forecast displacement error) and the OSSE framework were used in this study, a more comprehensive evaluation of the LBA effects on the real forecast are needed to show statistical confidence. Moreover, nature includes moist processes, which have stronger nonlinearity compared with dry processes, such as sea-breezes. This method should be verified for cases including precipitation to understand the case dependency.

6. Acknowledgements

We would like to thank the two anonymous reviewers for their constructive comments, which greatly improved the manuscript. The simulations were conducted using the Japan Meteorological Agency Nonhydrostatic Model (JMA-NHM) developed by the Meteorological Research Institute and the Numerical Prediction of the Japan Meteorological Agency. Some of the numerical experimental results of this work were obtained using supercomputing resources (NEC, SX-9) at the Cyberscience Center, Tohoku University. This study was supported by the Research Program on Climate Change Adaptation (RECCA) and (Cross-ministerial) Strategic Innovation Promotion Program (SIP) of the Ministry of Education, Culture, Sports, Science and Technology of Japan (MEXT) and a Grant-in-Aid for Scientific Research (21244074), 'Study of advanced data assimilation and cloud resolving ensemble technique for prediction of local heavy rainfall'.

References

Bishop, C. H., Etherton, B. J. and Majumdar, S. J. 2001. Adaptive sampling with the ensemble transform Kalman filter. Part I: theoretical aspects. *Mon. Weather Rev.* **129**, 420–436.

Errico, R. and Baumhefner, D. 1987. Predictability experiments using a high-resolution limited-area model. *Mon. Weather Rev.* **115**, 488–504.

Errico, R. M., Vukicevic, T. and Raeder, K. 1993. Comparison of initial and boundary condition sensitivity for a limited-area model. *Tellus A.* **45**, 539–557.

Frech, M., Holzäpfel, F., Tafferner, A. and Gerz, T. 2007. High-resolution weather database for the terminal area of Frankfurt airport. *J. Appl. Meteorol. Climatol.* **46**, 1913–1932.

Gaspari, G. and Cohn, S. E. 1999. Construction of correlation functions in two and three dimensions. *Q. J. Roy. Meteorol. Soc.* **125**, 723–757.

Gustafsson, N. 2012. Control of lateral boundary conditions in four-dimensional variational data assimilation for a limited area model. *Tellus A.* **64**, 17518.

Gustafsson, N., Kallen, E. and Thorsteinsson, S. 1998. Sensitivity of forecast errors to initial and lateral boundary conditions. *Tellus A*. **50**, 167–185.

Hamill, T. M., Whitaker, J. S. and Snyder, C. 2001. Distance-dependent filtering of background error covariance estimates in an ensemble Kalman filter. *Mon. Weather Rev*. **129**, 2776–2790.

Hunt, B. R., Kalnay, E., Kostelich, E. J., Ott, E., Patil, D. J. and co-authors. 2004. Four-dimensional ensemble Kalman filtering. *Tellus A*. **56**, 273–277.

Hunt, B. R., Kostelich, E. J. and Szunyogh, I. 2007. Efficient data assimilation for spatiotemporal chaos: a local ensemble transform Kalman filter. *Physica D*. **230**, 112–126. DOI: 10.1016/j.physd.2006.11.008.

Ishii, S., Sasaki, K., Mizutani, K., Aoki, T., Itabe T. and co-authors. 2007. Temporal evolution and spatial structure of the local easterly wind ''kiyokawa-dashi'' in Japan part i: coherent Doppler lidar observations. *J. Meteorol. Soc. Jpn*. **85**, 797–813.

Iwai, H., Ishii, S., Tsunematsu, N., Mizutani, K., Murayama Y. and co-authors. 2008. Dual-Doppler lidar observation of horizontal convective rolls and near surface streaks. *Geophys. Res. Lett*. **35**, L14808.

Iwai, H., Murayama, Y., Ishii, S., Mizutani, K., Ohno, Y. and co-authors. 2011. Strong updraft at a sea-breeze front and associated vertical transport of near-surface dense aerosol observed by Doppler lidar and ceilometer. *Bound. Layer Meteorol*. **141**, 117–142.

Kalnay, E. and Yang, S.-C. 2010. Accelerating the spin-up of ensemble Kalman filtering. *Q. J. Roy. Meteorol. Soc*. **136**, 1644–1651. DOI: 10.1002/qj.652.

Kawabata, T., Seko, H., Saito, K., Kuroda, T., Tamiya, K. and co-authors. 2007. An assimilation and forecasting experiment of the Nerima heavy rainfall with a cloud-resolving nonhydrostatic 4-dimensional variational data assimilation system. *J. Meteorol. Soc. Jpn*. **85**, 255–276.

Laprise, R., Varma, M. R., Denis, B., Caya, D. and Zawadzki, I. 2000. Predictability of a nested limited-area model. *Mon. Weather Rev*. **128**, 4149–4154.

Miyoshi, T. 2010. NHM-LETKF. *Tech. Rep. MRI*. **62**, 159–163.

Miyoshi, T. and Aranami, K. 2006. Applying a four-dimensional local ensemble transform Kalman filter (4D-LETKF) to the JMA nonhydrostatic model (NHM). *SOLA*. **2**, 128–131.

Miyoshi, T. and Kunii, M. 2012. The local ensemble transform Kalman filter with the weather research and forecasting model: experiments with real observations. *Pure Appl. Geophys*. **169**, 321–333.

Proctor, F. H., Hamilton, D. W., Rutishauser, D. K. and Switzer, G. F. 2004. *Meteorology and Wake Vortex Influence on American Airlines FL-587 Accident*. Technical Report 213018, Langley Research Center, NASA, 60 pp.

Saito, K., Ishida, J., Aranami, K., Hara, T., Segawa, T. and co-authors. 2007. Nonhydrostatic atmospheric models and operational development at JMA. *J. Meteorol. Soc. Jpn*. **85B**, 271–304.

Saito, K., Seko, H., Kunii, M. and Miyoshi, T. 2012. Effect of lateral boundary perturbations on the breeding method and the local ensemble transform Kalman filter for mesoscale ensemble prediction. *Tellus A*. **64**, 11594.

Seko, H., Kawabata, T., Tsuyuki, T., Nakamura, H., Koizumi, K. and co-authors. 2004. Impacts of GPS-derived water vapor and radial wind measured by Doppler radar on numerical prediction of precipitation. *J. Meteorol. Soc. Jpn*. **82**, 473–489.

Seko, H., Miyoshi, T., Shoji, Y. and Saito, K. 2011. Data assimilation experiments of precipitable water vapour using the LETKF system: intense rainfall event over Japan 28 July 2008. *Tellus A*. **63**, 402–414.

Shun, C. M. and Chan, P. W. 2008. Applications of an infrared Doppler lidar in detection of wind shear. *J. Atmos. Ocean. Technol*. **25**, 637–655.

Torn, R. D., Hakim, G. J. and Snyder, C. 2006. Boundary conditions for limited-area ensemble Kalman filters. *Mon. Weather Rev*. **134**, 2490–2502.

Warner, T. T., Peterson, R. A. and Treadon, R. E. 1997. A tutorial on lateral boundary conditions as a basic and potentially serious limitation to regional numerical weather prediction. *Bull. Am. Meteorol. Soc*. **78**, 2599–2617.

Yamamoto, K. 2009. Observation of non-precipitating low-level wind shear using the Doppler lidar for aviation weather. *Tenki*. **56**, 848–854 (in Japanese).

Yang, S.-C., Kalnay, E. and Hunt, B. 2012. Handling nonlinearity in an ensemble Kalman filter: experiments with the three-variable Lorenz model. *Mon. Weather Rev*. **140**, 2628–2646. DOI: 10.1175/MWR-D-11-00313.1.

Zou, X. and Kuo, Y.-H. 1996. Rainfall assimilation through an optimal control of initial and boundary conditions in a limited-area mesoscale model. *Mon. Weather Rev*. **124**, 2859–2882.